Frontiers of Physics
https://doi.org/10.1007/s11467-019-0932-1
Front. Phys.
14(6), 63604 (2019)

RESEARCH ARTICLE

Thermally activated phase transitions in Fe-Ni core-shell nanoparticles

Jin-Bo Wang, Rao Huang†, Yu-Hua Wen‡

Department of Physics, Jiujiang Research Institute and Collaborative Innovation Center for Optoelectronic Semiconductors and Efficient Devices, Xiamen University, Xiamen 361005, China
Corresponding authors. E-mail: †huangrao@xmu.edu.cn, ‡yhwen@xmu.edu.cn
Received May 29, 2019; accepted August 30, 2019

Fe-Ni core-shell nanoparticles are versatile functional materials, and their thermal stabilities are crucial for their performances in operating conditions. In this study, the thermodynamic behaviors of Fe-Ni core-shell nanoparticles are examined under continuous heating. The solid–solid phase transition from body centered cubic (*bcc*) to face centered cubic (*fcc*) in the Fe core is identified. The transition is accompanied with the generation of stacking faults around the core-shell interface, which notably lowers the melting points of the Fe-Ni core-shell nanoparticles and causes even worse thermal stability compared with Ni ones. Moreover, the temperature of the structural transformation is shown to be tuned by modifying the Ni shell thickness. Finally, the stress distributions of the core and the shell are also explored. The relevant results could be helpful for the design, preparation, and utilization of Fe-based nanomaterials.

Keywords core-shell, metallic, nanoparticle, phase transition, molecular dynamics

1 Introduction

As one of the most abundant and affordable metals on the earth, Fe has attracted intense interest because of its rich variety in possibilities of technological applications. With the size shrinking into the nanoscale, Fe nanoparticles become an important class of functional materials. They are extensively used in magnetic recording media [1], drug delivery [2], catalysis [3, 4], biomedical applications [5, 6], and environmental protection [7, 8]. However, there exists an intractable issue when Fe nanoparticles are exposed in operating conditions: they are prone to oxidation in the air and corrosion in solutions owing to their high reactivity. One of the resolution strategies is introducing another metal into Fe nanoparticles to form a bimetallic system. The investigations on this area have been in a boom over the past decades since it is an effective approach to modulate the physical and chemical properties of monometallic particles through both structure and composition designs.

Among all the candidates for the incorporated component, Ni becomes a natural choice owing to its superior stability, low cost, and ferromagnetism. Fe-Ni alloys are extensively used in diversified occasions including computer storage [9, 10], medical treatments with magnetic carriers involved [11], and catalytic reactions such as elective hydrogen generation from hydrous hydrazine, CO methanation, elimination of various pollutants [12–15]. The versatility of Fe-Ni bimetallic nanoparticles is closely associated with their structure and composition distribution, which may be sensitive to the ambient temperatures. Therefore, the thermal properties of these bimetallic nanoparticles would be a crucial issue since different temperatures may come into play in both synthesis and operating conditions. As is known, the thermal behaviors of bimetallic systems are much more complex than those of their monometallic counterparts because the presence of the second component breaks the structural symmetry, which results in further rugged energy landscapes. Given the fact that Fe is a representative metal of allotropy and the allotropic forms can transform from each other under certain temperature and pressure, alloying would additionally diversify the thermodynamic behaviors due to the presence of different chemical order or interfaces and lead to various possibilities in structural change or phase transition. However, to our knowledge, an in-depth understanding of the thermal properties of Fe-Ni bimetallic nanoparticles is still lacking. Hence, in this work we examine the dynamic evolution of their structures under continuous heating process and shed light on the structural transformations. This paper is structured as follows. In Section 2, the model construction of Fe-Ni nanoparticles and the computational methodology will be described. The calculated results for these nanoparticles will be discussed and be compared with available studies in Section 3, and finally, the main conclusions will be summarized in Section 4.

2 Simulation methodology

As illustrated in Fig. 1, Fe-core/Ni-shell (denoted as Fe@Ni) nanoparticles were produced from the bulks. Fe and Ni monometallic counterparts were also constructed

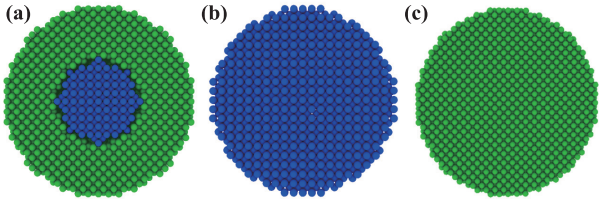

Fig. 1 Schematic illustrations of **(a)** Fe@Ni, **(b)** *bcc* Fe, and **(c)** *fcc* Ni nanoparticles. Coloring denotes the type of atom: blue, Fe atom; green, Ni atom.

for the purpose of comparison. According to the bulk crystalline structures, the initial configurations of Fe and Ni were respectively modeled to be body-centered-cubic (*bcc*) and face-centered-cubic (*fcc*). For the bimetallic nanoparticles, the Fe core is *bcc* lattice while the Ni shell belongs to *fcc* lattice. The number of atoms in the Fe core was set to be fixed at 947 (with a radius of about 1.5 nm), and different thicknesses of the Ni shell, ranging from 0.7 to 2.7 nm, were considered.

In this work, the interatomic interactions were described by the potentials developed by Bonny *et al.* [16], which are in the embedded atom method (EAM) formalism and their parameters were fitted with the emphasis on thermodynamics, defect energies, and vacancy migration barriers. These potentials were found to be able to reproduce the equilibrium phase diagram of Fe-Ni system that is in reasonable agreement with related experiments and have been extensively adopted in atomistic simulations of Fe-Ni alloys [17–19]. Therefore, we believe these thermodynamically validated potentials are suitable for the current investigation.

Before the simulations of heating, conjugate gradient method (CGM) was applied to quasi-statically relax all the initial configurations so as to reach the energy local minima. Thereafter, the nanoparticles were subjected to continuous heating, which was performed in a canonical ensemble, that is, the constant volume and temperature ensemble (NVT), using the molecular dynamics package LAMMPS. The temperature was gradually increased from 0 to 2000 K with an increment of 10 K. At each temperature, the relaxation time was set to be 200 ps, during which the atomic coordinates, velocities, and energies were extracted in the last 20 ps for the calculation of the statistical quantities.

3 Results and discussion

To identify the phase transitions during continuous heating, the temperature dependent potential energy and the corresponding heat capacity of Fe@Ni nanoparticles with different sizes are shown in Fig. 2. Note that the heat capacity may be deduced by the following equation [20]:

$$C_{\mathrm{p}}(T) = \frac{\mathrm{d}E}{\mathrm{d}T} + \frac{3}{2}R_{gc}, \tag{1}$$

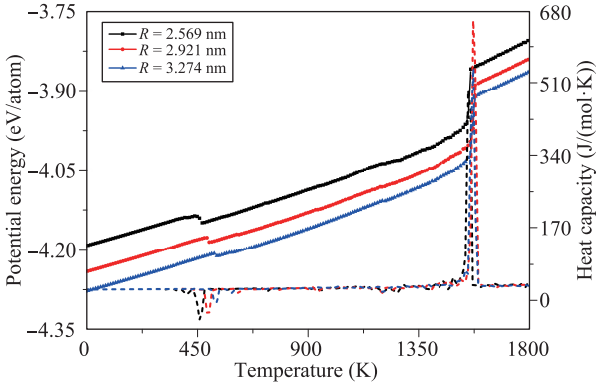

Fig. 2 Temperature dependence of potential energy (solid lines) and the corresponding heat capacities (dashed lines) for the Fe@Ni nanoparticles with three different sizes. Note that R denotes the particle radius.

where E is the potential energy, and $R_{\mathrm{gc}} = 8.314$ J/(mol K) is the ideal gas constant.

The abrupt increase in the potential energy and the sharp peak in the heat capacity signify the solid-liquid phase transition, i.e., melting. It occurs around 1500 K (to be specific, 1540, 1550, and 1560 K for the three nanoparticles, respectively). It has been well acknowledged that nanomaterials with large surface-to-volume ratios display lower melting points than their bulk counterparts because of the weaker bond of surface atoms comparing with the interior ones [20–24]. Considering that the bulk values of melting temperatures for Fe and Ni are respectively 1811 and 1728 K [25], the decrement of about 200 K in these nanoparticles should be reasonable. Meanwhile, slight drops are found around the temperature of 500 K in the potential energy curves. Accordingly, the heat capacity becomes negative here. Since this temperature region is far away from the melting point, Fe@Ni nanoparticles should be firmly in the solid regime. Therefore, these drops in energy curves indicate the occurrence of solid–solid phase transition. The critical temperatures are ascertained to be 450, 530, and 550 K for the three nanoparticles, increasing with the shell thickness. It can also be noted that this solid–solid phase transition in the Fe@Ni nanoparticles is explicitly induced by the core-shell configuration because it is absent in both pure Fe and Ni nanoparticles. These two types of first-order phase transitions will be elaborated later.

The melting points of Fe@Ni nanoparticles with different sizes are exhibited in Fig. 3, in which the corresponding values for pure Fe and Ni equivalents are also presented for reference. Originated from the impact of the surface-to-volume ratio, the size effect can be clearly identified from this figure. However, the trend becomes much less distinct as the particle radius is larger than 3.5 nm, and further elevated melting temperature could only be realized when the size increases substantially. Generally, the melting points of bimetallic systems lie in between those of

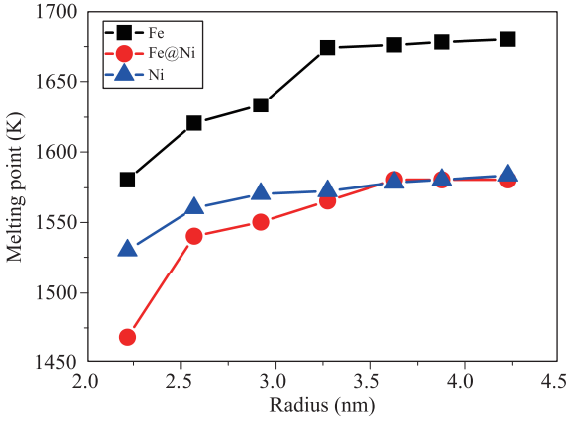

Fig. 3 Size-dependent melting points of Fe@Ni, Fe, and Ni nanoparticles.

their monometallic counterparts and depend on the composition ratio [26]. Nevertheless, it is not the case here. It can be found from Fig. 3 that the melting temperatures for the smaller sized Fe@Ni nanoparticles are even lower than their pure Ni counterparts. As the thickness of Ni shell grows and the particle radius exceeds 3.5 nm, Fe@Ni and pure Ni nanoparticles melt at the identical temperature, i.e., the influence induced by the existence of the Fe core becomes inconspicuous. Therefore, it is reasonable to suppose that the abnormally lowered melting points in the Fe@Ni nanoparticles should be associated with the solid–solid phase transition, which is revealed by Fig. 2 and is absent in the pure Fe or Ni nanoparticles.

In order to visualize the phase transitions occurring during the heating process, common neighbor analysis (CNA) [27] was adopted to characterize the local crystal structure in the nanoparticles. It is a decomposition of the radial distribution function (RDF) according to the local environment of the pairs of atoms and can be used to identify atoms in particular order, such as *fcc*, *bcc*, and hexagonal close-packed (*hcp*). Take the Fe@Ni nanoparticle with the radius of about 3.6 nm (including 17831 atoms) for example, Fig. 4 shows its structural evolution with increasing temperature. Owing to the relatively large difference in the lattice structures and the lattice constants between Fe and Ni (2.87 Å for the former and 3.52 Å for the latter), the lattice misfit is considerable and thus leads to an appreciable amount of "other" atoms located near the core-shell interface [see Fig. 4(a)]. With the temperature increasing, the Fe core turns from spherical to ellipsoidal at 500 K, which implies the initiation of the solid–solid phase transition and could be corroborated from the potential energy curve in Fig. 2. Hereafter, it can be ascertained by the CNA method that the original *bcc* Fe atoms transform into *fcc* ones. From the values of potential energies in Fig. 2, one may find that the *fcc* configuration actually is more stable than *bcc* for the Fe core. From the analysis of the intermediate states between the *bcc* and *fcc* phases of the Fe core, the transformation is observed to occur through complex processes. The corresponding pathways are similar to the Nishiyama–Wassermann path rather than the Bain path. Actually, there has been a comparison between the Bain and Nishiyama–Wassermann paths in bulk Fe, and the results showed that the martensite transformation rather follows the Nishiyama–Wassermann path in reality [28]. Therefore, we believe it is reasonable to find that the Bain pathway is absent in our investigation. Meanwhile, it should be noted that, owing to the existence of the surface (or interface), the transformation path could be far more complex in the clusters than that in the bulk. The standard paths may be distorted in different degrees depending on the lattice distance from the surface (or interface). Furthermore, it can be seen that this structural transformation is accompanied by a few *hcp* atoms appearing near the periphery of the core, which correspond to stacking faults as shown in Fig. 4(c). These stacking faults further expand with elevated temperature, and some of them even penetrate the entire nanoparticle arriving at the surface [see Figs. 4(d) and (e)]. The existence of these stacking faults is exactly the cause of the reduced thermal stability of Fe@Ni nanoparticles comparing with the monometallic Ni ones, which has also been observed in other bimetallic systems such as Pt-Au [29] and Pd-Ni [30]. Since the emergence of the stacking faults is triggered by the solid–solid phase transition in the Fe core, it is natural to find that its influence on the melting point would become smaller with increasing shell thickness for the fixed core size, as shown in Fig. 3.

According to the observation that the solid–solid phase transition is absent in the monometallic *bcc* Fe and *fcc* Ni nanoparticles, it is sensible to consider that the structural transformation is introduced by the inconsistent lattice in the core-shell interface. Here we calculated the atomic stress during heating. The local stress δ_n at the i_{th} atom site can be calculated by

$$\delta_n = \frac{1}{3}\sum_{\alpha=1}^{3}\delta_{\alpha\alpha} = \frac{1}{3}\sum_{\alpha=1}^{3}\left(\frac{1}{2\Omega_i}\sum_{j\neq i}F_{ij}^{\alpha}R_{ij}^{\alpha}\right), \tag{2}$$

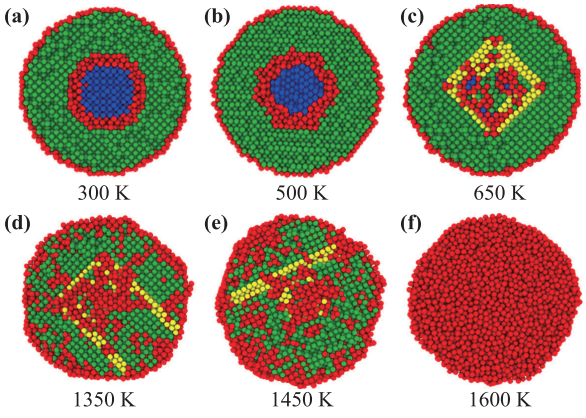

Fig. 4 Cross-sectional snapshots of the Fe@Ni nanoparticle taken at six representative temperatures. Colors denote atomic types: blue, *bcc*; yellow, *hcp*; green, *fcc*; red, other.

in which F_{ij} and R_{ij} are the force and distance between atoms i and j, respectively [31]. Ω_i is the local volume that can be identified with the volume of the Voronoi polyhedra constructed by the perpendicular planes that bisect the lines between atom i and all its neighbor atoms, which has been calculated through the equal volume method [32]. Figure 5 presents the stress distribution in the Fe@Ni nanoparticle exemplified in Fig. 4. The values at two temperatures (respectively before and after the solid–solid transition) are illustrated in Figs. 5(a) and (b). Evidently, the tangential stresses of outermost Ni atoms are positive because of surface tension. However, when all the atoms are taken into account to calculate the average values, the Ni shell is under compression, and the Fe core is subjected to tensile stress. It is opposite to the situation in monometallic particles where the surface is in tension and the interior region is generally compressive [33, 34]. This reversed trend is due to the fact that the lattice constant of Fe (2.87 Å) is much smaller than that of Ni (3.52 Å). The lattice accommodation thus builds up the stress gap between the core and the shell, and comparing to the surface, the existence of core-shell interface plays a more dominant role in determining the stress distribution of the whole particle. Before the structural transition of *bcc* Fe core (occurs at 570 K), the gap between the average stresses of the two components is 24.9 MPa. After the transition, the stress gap is lowered to 22.9 MPa, not notably but still implying the release of the stress.

To further explore the relationship between the atomic stress and the solid–solid phase transition in the Fe core, the average stress and the critical temperature of the phase transition at different Ni shell thicknesses are demonstrated in Fig. 6. As the Ni shell thickness increases from about 1.1 to 2.4 nm, the Fe core is always subjected to tensile stress, and the average value also increases from 21.6 to 31.7 MPa. The stress rise is because the lattice

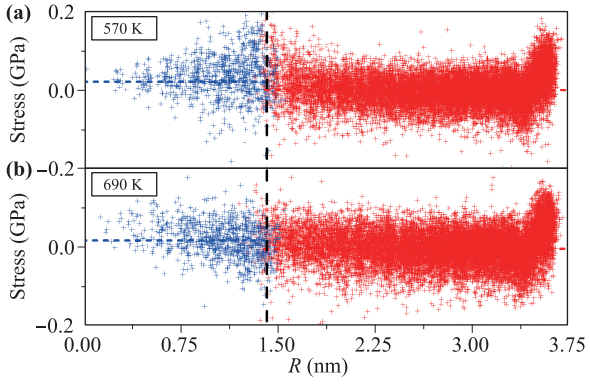

Fig. 5 Stress distribution in the Fe@Ni nanoparticle before (570 K) and after (690 K) the solid–solid phase transition of the Fe core. The horizontal axis represents the distance of the atom from the center of the mass. The horizontal dashed lines indicate the average stresses in the shell and the core, respectively.

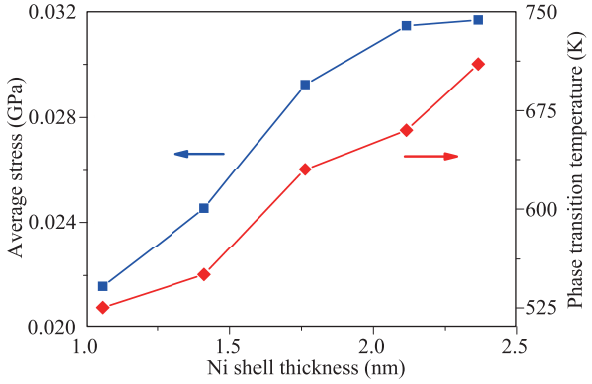

Fig. 6 Ni shell thickness dependent average stress under room temperature of 300 K and the solid–solid phase transition temperature in the Fe core.

expansion of the Fe atoms is originated from the attempt at accommodating to the Ni lattice in the core-shell interface. Thick shell results in enhanced tension imposed on Fe core. As for the transition temperature of *bcc* to *fcc* phase, it elevates from 525 to 710 K. As is known, under the standard atmosphere pressure, Fe exhibits *bcc* structure from room temperature to 1185 K, while *fcc* structure between 1185 and 1667 K [28, 35]. However, according to our calculations, when its size falls into nanoscale and it is covered by Ni shell, the critical temperature significantly drops and is tunable by controlling the shell thickness. This observation, which discloses the thermodynamic behaviors of *bcc* Fe in nanoparticles that are profoundly different from the bulk situation, provides a promising strategy of designing Fe based nanomaterials with different crystalline phases.

4 Conclusions

In summary, molecular dynamics simulations were employed to investigate the thermodynamic behaviors of Fe@Ni bimetallic nanoparticles. During continuous heating, the solid–solid phase transition from *bcc* to *fcc* was observed in the Fe core. This change in crystalline structure leads to the occurrence of stacking faults near the core-shell interface, which significantly reduces the thermal stability of these nanoparticles and results in the melting points even lower than pure Ni counterparts. Moreover, the *bcc* Fe cores are found to be subjected to tensile stress in the Fe@Ni nanoparticles due to lattice misfit, and the stress is released to a certain extent after the structural transformation. Both the initial stress and the critical temperature of the solid–solid phase transition in the core increase with the shell thickness. These results, which may be expanded to systems with *bcc* Fe cores covered by other *fcc* metallic shells, provide a theoretical reference for both the synthesis and application of Fe-based nanomaterials.

Acknowledgements This work was supported by the National Natural Science Foundation of China (Grant Nos. 11474234 and 51871189).

References

1. V. Amendola, P. Riello, and M. Meneghetti, Magnetic nanoparticles of iron carbide, iron oxide, iron@iron oxide, and metal iron synthesized by laser ablation in organic solvents, *J. Phys. Chem. C* 115(12), 5140 (2011)
2. D. L. Huber, Synthesis, properties, and applications of iron nanoparticles, *Small* 1(5), 482 (2005)
3. Z. Y. Zhou, N. Tian, J. T. Li, I. Broadwell, and S. G. Sun, Nanomaterials of high surface energy with exceptional properties in catalysis and energy storage, *Chem. Soc. Rev.* 40(7), 4167 (2011)
4. Y. X. Chen, S. P. Chen, Z. Y. Zhou, N. Tian, Y. X. Jiang, S. G. Sun, Y. Ding, and Z. L. Wang, Tuning the shape and catalytic activity of Fe nanocrystals from rhombic dodecahedra and tetragonal bipyramids to cubes by electrochemistry, *J. Am. Chem. Soc.* 131(31), 10860 (2009)
5. L. M. Lacroix, N. F. Huls, D. Ho, X. L. Sun, K. Cheng, and S. H. Sun, Stable single-crystalline body centered cubic Fe nanoparticles, *Nano Lett.* 11(4), 1641 (2011)
6. A. K. Gupta and M. Gupta, Synthesis and surface engineering of iron oxide nanoparticles for biomedical applications, *Biomaterials* 26(18), 3995 (2005)
7. X. Zhao, W. Liu, Z. Q. Cai, B. Han, T. W. Qian, and D. Y. Zhao, An overview of preparation and applications of stabilized zero-valent iron nanoparticles for soil and groundwater remediation, *Water Res.* 100, 245 (2016)
8. T. Phenrat, D. Schoenfelder, T. L. Kirschling, R. D. Tilton, and G. V. Lowry, Adsorbed poly(aspartate) coating limits the adverse effects of dissolved groundwater solutes on Fe^0 nanoparticle reactivity with trichloroethylene, *Environ. Sci. Pollut. Res. Int.* 25(8), 7157 (2018)
9. A. P. Douvalis, R. Zboril, A. B. Bourlinos, J. Tucek, S. Spyridi, and T. Bakas, A facile synthetic route toward air-stable magnetic nanoalloys with Fe–Ni/Fe–Co core and iron oxide shell, *J. Nanopart. Res.* 14(9), 1130 (2012)
10. S. F. Moustafa and W. M. Daoush, Synthesis of nano-sized Fe-Ni powder by chemical process for magnetic applications, *J. Mater. Process. Technol.* 181(1–3), 59 (2007)
11. P. Tartaj, M. P. Morales, S. Veintemillas-Verdaguer, T. González-Carreño, and C. J. Serna, The preparation of magnetic nanoparticles for applications in biomedicine, *J. Phys. D Appl. Phys.* 36(13), R182 (2003)
12. S. K. Sanjay, A. K. Singh, K. Aranishi, and Q. Xu, Noble-metal-free bimetallic nanoparticle-catalyzed selective hydrogen generation from hydrous hydrazine for chemical hydrogen storage, *J. Am. Chem. Soc.* 133(49), 19638 (2011)
13. S. A. Theofanidis, V. V. Galvita, H. Poelman, and G. B. Marin, Enhanced carbon-resistant dry reforming Fe-Ni catalyst: Role of Fe, *ACS Catal.* 5(5), 3028 (2015)
14. Y. H. Tee, L. Bachas, and D. Bhattacharyya, Degradation of trichloroethylene by iron-based bimetallic nanoparticles, *J. Phys. Chem. C* 113(22), 9454 (2009)
15. M. Rivero-Huguet and W. D. Marshall, Reduction of hexavalent chromium mediated by micro- and nano-sized mixed metallic particles, *J. Hazard. Mater.* 169(1–3), 1081 (2009)
16. G. Bonny, R. C. Pasianot, and L. Malerba, Fe-Ni many-body potential for metallurgical applications, *Model. Simul. Mater. Sci. Eng.* 17(2), 025010 (2009)
17. K. Vörtler, N. Juslin, G. Bonny, L. Malerba, and K. Nordlund, The effect of prolonged irradiation on defect production and ordering in Fe-Cr and Fe-Ni alloys, *J. Phys.: Condens. Matter* 23(35), 355007 (2011)
18. N. Anento, A. Serra, and Y. Osetsky, Effect of nickel on point defects diffusion in Fe-Ni alloys, *Acta Mater.* 132, 367 (2017)
19. C. G. Zhang, K. Ma, N. Q. Zhao, and Z. H. Yuan, A core-shell strategy for improving alloy catalyst activity for continual growth of hollow carbon onions, *Cryst. Growth Des.* 18(12), 7470 (2018)
20. Y. Qi, T. Cagin, W. L. Johnson, and W. A. III Goddard, Melting and crystallization in Ni nanoclusters: The mesoscale regime, *J. Chem. Phys.* 115(1), 385 (2001)
21. R. Huang, Y. H. Wen, Z. Z. Zhu, and S. G. Sun, Thermal stability of platinum nanowires: a comparison study between single-crystalline and twinned structures, *J. Mater. Chem.* 21(47), 18998 (2011)
22. Q. S. Mei and K. Lu, Melting and superheating of crystalline solids: from bulk to nanocrystals, *Prog. Mater. Sci.* 52(8), 1175 (2007)
23. Y. Shibuta and T. Suzuki, Melting and nucleation of iron nanoparticles: A molecular dynamics study, *Chem. Phys. Lett.* 445(4–6), 265 (2007)
24. R. Huang, Y. H. Wen, Z. Z. Zhu, and S. G. Sun, Structure and stability of platinum nanocrystals: From low-index to high-index facets, *J. Mater. Chem.* 21(31), 11578 (2011)
25. C. Kittel, Introduction to Solid State Physics, John Wiley & Sons Press, 1956
26. R. Huang, Y. H. Wen, Z. Z. Zhu, and S. G. Sun, Pt-Pd bimetallic catalysts: Structural and thermal stabilities of core-shell and alloyed nanoparticles, *J. Phys. Chem. C* 116(15), 8664 (2012)
27. J. D. Honeycutt and H. C. Andersen, Molecular-dynamics study of melting and freezing of small Lennard–Jones clusters, *J. Phys. Chem.* 91(19), 4950 (1987)
28. L. Sandoval, H. M Urbassek, and P. Entel, The Bain versus Nishiyama–Wassermann path in the martensitic transformation of Fe, *New J. Phys.* 11(10), 103027 (2009)
29. R. Huang, S. F. Shao, X. M. Zeng, and Y. H. Wen, Diverse melting modes and structural collapse of hollow bimetallic core-shell nanoparticles: A perspective from molecular dynamics simulations, *Sci. Rep.* 4(1), 7051 (2015)

30. R. Huang, Y. H. Wen, Z. Z. Zhu, and S. G. Sun, Atomic-scale insights into structural and thermodynamic stability of Pd-Ni bimetallic nanoparticles, *Phys. Chem. Chem. Phys.* 18(14), 9847 (2016)

31. C. Mottet, G. Rossi, F. Baletto, and R. Ferrando, Single impurity effect on the melting of nanoclusters, *Phys. Rev. Lett.* 95(3), 035501 (2005)

32. D. Srolovitz, K. Maeda, V. Vitek, and T. Egami, Structural defects in amorphous solids Statistical analysis of a computer model, *Philos. Mag. A* 44(4), 847 (1981)

33. Y. T. Cheng, and M. W. Verbrugge, The influence of surface mechanics on diffusion induced stresses within spherical nanoparticles, *J. Appl. Phys.* 104(8), 083521 (2008)

34. V. I. Levitas and K. Samani, Size and mechanics effects in surface-induced melting of nanoparticles, *Nat. Commun.* 2(1), 284 (2011)

35. H. Hasegawa and D. G. Pettifor, Microscopic theory of the temperature-pressure phase diagram of iron, *Phys. Rev. Lett.* 50(2), 130 (1983)